

Activated and nitrogen-doped exfoliated graphene as air electrodes for metal–air battery applications†

Cite this: *J. Mater. Chem. A*, 2013, **1**, 2639

Drew Higgins,‡ Zhu Chen,‡ Dong Un Lee and Zhongwei Chen*

Capitalizing on the immense theoretical energy storage densities of metal–air batteries requires the development of high performance air electrode materials. These materials must simultaneously meet the criteria of high surface areas, excellent oxygen reduction reaction activity and low cost. Herein, catalyst materials with exemplary surface areas ($2980 \text{ m}^2 \text{ g}^{-1}$) and ORR activity were developed by innovatively coupling KOH activation of exfoliated graphene with ammonia induced nitrogen doping (N-a-ex-G). Specifically, ORR activity approaching that of commercial platinum based catalysts was observed (ca. 45 mV lower onset potential), and these unique materials were found to provide excellent practical metal–air battery performance. In particular, N-a-ex-G provided a 60% higher discharge current (on a catalyst mass basis at a cell voltage of 1.0 V) in a zinc–air battery single cell, along with higher discharge voltages and a 42% capacitance increase in comparison with pure carbon black based electrodes in a Li–oxygen battery single cell. These promising results, attributed to the favourable properties of N-a-ex-G, including high surface areas and inherent ORR activity indicate their practicality as air cathode electrocatalysts.

Received 2nd November 2012
Accepted 18th December 2012

DOI: 10.1039/c2ta00944g

www.rsc.org/MaterialsA

1 Introduction

Surging global energy demands and rapidly depleting fossil fuel reserves have stimulated extensive interest in the research and development of electrochemical energy storage solutions¹ for use in electric/hybrid vehicles, portable electronics and smart grid infrastructures. In order to be technologically and commercially competitive on a global scale, improvements to the energy storage densities are required along with the simultaneous reduction in overall component and production costs. Metal–air batteries, including zinc–air and lithium–oxygen batteries, are emerging as promising replacements to traditionally utilized lithium-ion batteries, boasting theoretical energy storage densities of 1084 and 11 680 W h kg⁻¹, respectively.² These energy storage capabilities are orders of magnitude higher than lithium-ion batteries (200 W h kg⁻¹), and will be required in order to meet the intensive demands of modern and future applications. At the current state of technology, the practical energy densities of zinc–air and lithium–oxygen batteries are still limited by the electrode active materials

utilized. As the rate of the oxygen reduction reaction (ORR) is inherently much slower than the rate of the metal anode oxidation, the performance of these devices is governed by the air electrode catalyst materials. Moreover, commonly utilized ORR electrocatalysts rely on noble metals, such as platinum, or transition metal oxides that bear high costs and limited natural supply. Developing unique low cost air electrode catalyst technologies that rely on environmentally inexhaustible supplies will ensure long term sustainability, along with alleviating the breadth of environmental concerns associated with the production of metal based catalysts.³ Furthermore, ensuring high ORR activity of these materials is essential in order to capitalize on the exemplary theoretical energy storage densities of metal–air batteries resulting in high performance devices that are practical for numerous applications.

Unique graphene materials consisting of single sheets of carbon atoms are considered to be promising for many applications including electrocatalysis owing to their exemplary surface areas, high electronic conductivity, and robust thermal, mechanical and chemical stability.⁴ The inherent oxygen adsorption and reduction activity of pristine graphitic carbons is relatively poor, which can be overcome by the incorporation of heterogeneous nitrogen atoms into the graphitic structure.^{5–13} Moreover, nitrogen-doping of graphene (N-G) has been demonstrated to provide enhanced electronic properties, including enhanced conductivity and modulated electron densities that are attractive for electrocatalyst purposes. Currently however, the surface areas of the prepared N-G materials have been limited to approximately 500–600 m² g⁻¹,^{14,15} well below the theoretical

Department of Chemical Engineering, Waterloo Institute for Nanotechnology, Waterloo Institute for Sustainable Energy, University of Waterloo, Waterloo, ON, Canada, N2L 3G1. E-mail: zhwchen@uwaterloo.ca; Fax: +1 519-746-4347; Tel: +1 519-888-4567 ext. 38664

† Electronic supplementary information (ESI) available: Supplementary physicochemical characterization, electrochemical characterization and details of practical metal–air battery performance evaluation. See DOI: 10.1039/c2ta00944g

‡ Indicates joint first authorship.

surface area of completely exfoliated graphene sheets ($2630 \text{ m}^2 \text{ g}^{-1}$).⁴ As surface area is an important factor governing electrocatalyst activity,¹⁶ increasing the surface area of N-G catalyst materials offers a very promising approach for the development of new generation metal–air battery catalyst technologies.

Recently, Zhu *et al.*¹⁷ reported a potassium hydroxide (KOH) chemical activation of exfoliated graphene (ex-G) to produce activated (a-ex-G) materials with exemplary measured surface areas in excess of $3000 \text{ m}^2 \text{ g}^{-1}$, along with a high degree of micro- and mesoporosity. Herein, this technique is innovatively coupled with post-treatment nitrogen doping of a-ex-G (N-a-ex-G) by an ammonia thermal treatment. The result was N-a-ex-G materials possessing exemplary surface areas and high ORR activity approaching that of commercial platinum based catalysts. Owing to the attractive properties of the developed N-a-ex-G materials, excellent cathode catalyst performance in zinc–air and lithium–oxygen batteries was obtained. Ideally, the fabrication of N-a-ex-G relies on environmentally abundant materials, is straightforward and ideal for up-scalability to meet market demands. This technique is reported as a viable method to simultaneously optimize multiple aspects of graphene's properties that have the potential for utilization in high performance metal–air battery technologies.

2 Experimental methods and techniques

2.1 Synthesis of N-a-ex-G

Graphite oxide (GO) was synthesized by a modified Hummer's method.¹⁸ Briefly, 2 g of graphite powder and 1 g of sodium nitrate were combined in a round bottom flask. While stirring in an ice bath, 46 mL of concentrated sulfuric acid was added to the flask, followed by the slow addition of 6 g of potassium permanganate over 1 hour. The flask was then removed from the ice bath, stirred for 1 h at room temperature, and followed by the dropwise addition of 92 mL of distilled de-ionized (DDI) water. After stirring further for 30 minutes, the solution was diluted with 280 mL of warm DDI water along with 40 mL of 30% hydrogen peroxide to neutralize any remaining permanganate. The product was filtered and washed with copious amounts of 5% hydrochloric acid (HCl), followed by centrifugation and drying at room temperature under a gentle supply of flowing air. After collection, GO was thermally reduced and exfoliated (ex-G) by a thermal treatment method. GO was loaded into an alumina boat that was subsequently placed into a horizontal tube furnace reactor saturated with argon (100 sccm). Keeping GO out of the heating area, the furnace was heated to $1000 \text{ }^\circ\text{C}$, upon which the sample was pushed into the central heating zone where it remained for 30 seconds to obtain ex-G.

The collected ex-G was then chemically activated (a-ex-G) by KOH impregnation and subsequent heat treatment.^{17,19,20} First, ex-G was well dispersed in 3.5 M KOH under stirring for 4 hours and stagnated for 18 hours to allow KOH impregnation. The solution was then filtered and dried at $60 \text{ }^\circ\text{C}$ overnight. The dried product was placed into a horizontal tube furnace saturated with argon (100 sccm) and heated to $900 \text{ }^\circ\text{C}$ at a rate of $5 \text{ }^\circ\text{C min}^{-1}$. The temperature was maintained for 1 hour,

followed by cooling, sample removal and thorough washing with DDI water and ethanol in order to remove any unwanted residues and byproducts. After drying, nitrogen doping of a-ex-G (N-a-ex-G) was carried out by heat treatment in an ammonia environment. a-ex-G was placed into a horizontal tube furnace and heated to $900 \text{ }^\circ\text{C}$ under argon saturation (100 sccm). Once the furnace reached $900 \text{ }^\circ\text{C}$, ammonia was introduced under a constant rate of 50 sccm and held for 1 hour. After 1 hour, the ammonia supply was cut off and the furnace was cooled down to room temperature for sample collection.

2.2 Physicochemical characterization

Material characterization was carried out by a number of different techniques. Scanning electron microscopy (SEM, LEO FESEM 1530) and transmission electron microscopy (TEM, JEOL 2010F) images were obtained in order to investigate the morphology and surface features of the developed materials. X-ray diffraction (XRD) was carried out using on a Bruker AXS D8 Advance using Cu K α radiation with a wavelength of 1.54 Angstroms. X-ray photoelectron spectra (XPS) were obtained on a Thermo Scientific K-Alpha XPS spectrometer, using a monochromatic Al K α X-ray source with a take-off angle of 90° and a spot area of $400 \text{ }\mu\text{m}$. Brunauer–Emmett–Teller (BET) surface analysis was carried out using an Autosorb from Quantochrome Instruments. Nitrogen adsorption isotherms were obtained to gain insight regarding the surface areas and pore size distribution of the synthesized catalyst. Raman spectroscopy was carried out to track changes in the graphitic ordering of the samples through all stages of synthesis.

2.3 Electrochemical and practical battery cell testing

Electrochemical half-cell testing included linear sweep voltammetry (LSV) using a rotating ring disc voltammetry setup consisting of a biopotentiostat (Pine Instrument Co., AFCBP-1) and a rotator (Pine Instrument Co., AFMSRCE). A 5 mm OD glassy carbon electrode was coated with the catalyst sample and used as the working electrode, immersed in a glass cell containing 0.1 M KOH, a platinum wire counter electrode and a double junction Ag/AgCl reference electrode. Catalyst materials were deposited onto the working electrode first by preparing a 0.5 wt % Nafion in ethanol catalyst ink with a concentration of 4 mg catalyst per 1 mL of solution. The solution was sonicated for 1 hour to ensure a homogeneous dispersion, and then a $10 \text{ }\mu\text{L}$ aliquot was deposited onto the electrode surface and allowed to dry under ambient conditions. To remove capacitive contributions during evaluation of ORR activity, background currents were obtained under nitrogen saturated environments by sweeping the potential from 0.2 to $-1.0 \text{ V vs. Ag/AgCl}$ at a scan rate of 10 mV s^{-1} . These background contributions were subtracted from ORR polarization curves obtained under oxygen saturated conditions.

Evaluation of practical catalyst performance in a zinc–air single cell battery was facilitated using a multichannel potentiostat (Princeton Applied Research, VersaSTAT MC) and a home-made zinc–air battery setup. The air electrode was fabricated by coating catalyst materials onto a gas diffusion layer

(Ion Power Inc., SGL Carbon 10 BB) with an active electrode surface area of 2.84 cm^2 . The catalyst materials were dispersed into an isopropanol–Nafion mixture at a catalyst concentration of 9.4 mg mL^{-1} . The ink, containing a catalyst to Nafion weight ratio of approximately 3.6 : 1, was then air brush sprayed onto the gas diffusion layer and dried for subsequent testing. A polished zinc plate (OnlineMetals, Zinc Sheet EN 988) and a microporous $25 \text{ }\mu\text{m}$ polypropylene membrane (Celgard 5550) were used as the zinc electrode and separator, respectively. The electrolyte used in the zinc–air battery was 6 M KOH, an optimized concentration chosen based on results from a previous study.²¹ Battery discharge performances were measured by applying a galvanodynamic technique and polarization curves of the air electrode were collected for analysis. Electrochemical impedance spectroscopy was also utilized using AC frequencies from 0.1 Hz to 100 kHz with an amplitude of 20 mV. Data were fitted using ZSimpWin 3.10.

In order to evaluate the practical electrochemical performances of the developed catalyst materials in a lithium–oxygen battery, Swagelok type cells were prepared utilizing lithium metal as an anode and 1 M LiPF₆ in tetraethylene glycol dimethyl ether (TEGDME) as the electrolyte. The air cathode consists of N-a-ex-G as a catalyst, ketjen black (KB) as a supporting material, a copolymer of vinylidene fluoride with hexafluoropropylene (PVDF–HFP) as a binder, and dibutyl phthalate as a pore forming agent following procedures disclosed in a previous report.²² The carbon electrode materials contained a 20 : 80 weight ratio of N-a-ex-G and KB mixture, and the binder was incorporated with a 2.4 : 1 binder to carbon weight ratio. For comparison, an air electrode was fabricated with pure KB with the same binder content. Galvanostatic testing was carried out in order to evaluate the practical performance by applying a current density of 70 mA g^{-1} with a cut off voltage of 2.0 V under 1 atm oxygen atmosphere.

3 Results and discussion

SEM (Fig. S1†) and TEM (Fig. 1) images are provided to track the morphological changes occurring during the different stages of

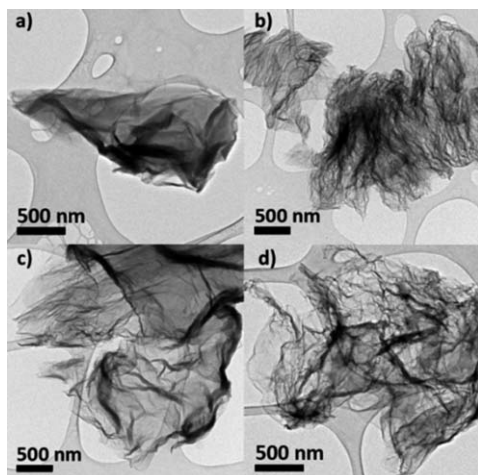


Fig. 1 TEM image of (a) GO, (b) ex-G, (c) a-ex-G, and (d) N-a-ex-G.

N-a-ex-G catalyst synthesis. Synthesized GO (Fig. 1a and S1a†) possesses a smooth, layered structure containing several stacked graphitic sheets that were converted to an agglomerated voile-like structure with clear indication of graphene sheet separation by thermal exfoliation (Fig. 1b and S1b†). Following activation (Fig. 1c and S1c†) and nitrogen doping (Fig. 1d and S1d†) significant agglomeration is no longer observed, and the separated graphene sheets possess a highly wrinkled morphology. The nitrogen adsorption/desorption curves (Fig. S2†) indicated the presence of a large number of micro and macropores, demonstrating a Type IV isotherm with a type H3 hysteresis loop.²³ The BET apparent surface area of N-a-ex-G calculated from the adsorption isotherm was determined to be $2980 \text{ m}^2 \text{ g}^{-1}$, exceeding the theoretical surface area of pristine graphene. This is slightly lower than the surface area of $3100 \text{ m}^2 \text{ g}^{-1}$ reported previously for KOH activated microwave exfoliated graphene,¹⁷ which can be attributed to different processing techniques.

Surface elemental compositions determined by XPS are summarized in Table 1, along with high resolution C1s and N1s spectra for N-a-ex-G provided in Fig. 2. C1s peaks for all samples are provided in the ESI (Fig. S3†) along with appropriate discussion of the changes occurring during catalyst synthesis. Following ammonia treatment, the surface nitrogen concentration of N-a-ex-G was 1.57 at.%. This confirmed successful nitrogen incorporation, although the nitrogen content was slightly lower in comparison to previously reported ammonia treated thermally exfoliated graphene^{7,14} which is reasonable considering the reduced amount of oxygen sites available after activation that can facilitate nitrogen incorporation.⁶ Although increased nitrogen contents have been linked to enhanced ORR activity,^{24,25} the activated, open pore structure of N-a-ex-G can offer easily accessible ORR active sites to promote activity even at relatively lower nitrogen content.

The N1s spectra of N-a-ex-G (Fig. 2b) were deconvoluted into four contributing peaks including: (i) pyridinic (398.2 eV), (ii) pyrrolic (399.6 eV), (iii) quaternary (401.0 eV) and (iv) oxidized (402.9 eV) nitrogen functionalities present in varying amounts.

Although the exact ORR contributions of the various nitrogen groups are debatable, the strong presence of pyridinic and quaternary nitrogen have been linked to ORR activity^{26–28} and can provide logical explanation for the performance enhancements discussed hereafter. Further work is directed at elucidating the exact nature of the ORR active site moieties and tailoring catalyst designs accordingly.

Successful nitrogen doping was further confirmed by Raman spectroscopy, with the Raman spectra for all samples provided in Fig. 3. This figure illustrates two bands located at *ca.* 1345 and 1583 cm^{-1} , attributed to the D band and the G band,

Table 1 XPS determined surface compositions of graphene samples

Element	GO (at.%)	ex-G (at.%)	a-ex-G (at.%)	N-a-ex-G (at.%)
C	66.03	92.51	95.49	96.84
N	—	—	—	1.57
O	33.97	7.49	4.51	1.59

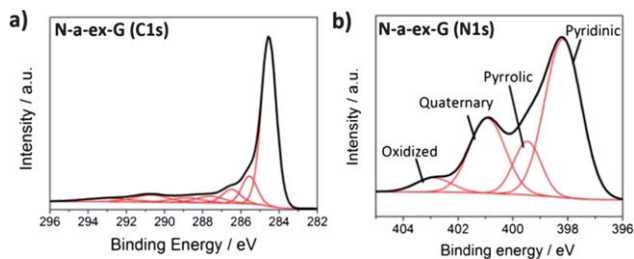


Fig. 2 High resolution XPS (a) C1s and (b) N1s signal of N-a-ex-G.

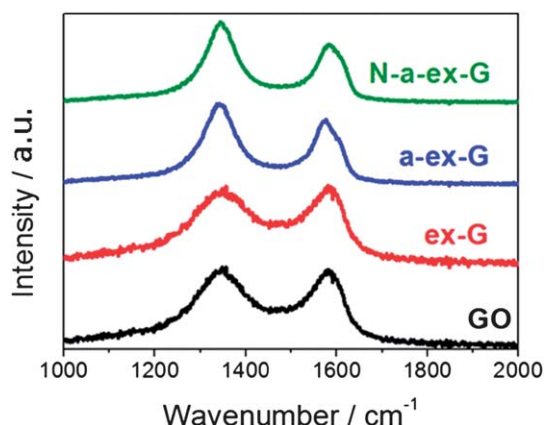


Fig. 3 Raman spectroscopy of graphene samples throughout all stages of catalyst synthesis.

respectively. The D band arises due to the structural disorder or defects present in graphitic based samples; whereas the G band arises from sp^2 bonded ordered graphitic carbon.²⁹ The ratio of D to G band intensity (I_D/I_G) is commonly utilized to gauge the degree of structural disorder present, with higher values indicating more disorder along with smaller inter defect distances and average graphitic crystalline sizes.³⁰ GO illustrates a near unity I_D/I_G of 1.03, a common observation for this class of material.²⁹ Following thermal exfoliation, a decrease in the I_D/I_G band to 0.94 was observed for ex-G due to removal of the oxygen functionalities and reversion to a more ordered graphitic structure. Chemical activation resulted in an increase of the I_D/I_G ratio to 1.25, consistent with a previous report¹⁷ and attributed primarily to removal of carbon species by KOH resulting in smaller crystallite sizes and a higher degree of bond angle disorder.³¹ Lastly, following nitrogen doping, the I_D/I_G ratio of N-a-ex-G increased further to 1.42, a consistently reported observation due to nitrogen defect incorporation.^{14,32,33}

Half-cell testing was utilized to evaluate graphene based material's ORR kinetics in an O_2 saturated 0.1 M KOH electrolyte (Fig. 4a and S5–S8†). Samples were found to possess increasing activity in the order of $GO < ex-G < a-ex-G < N-a-ex-G$. In comparison to the negligible activity demonstrated by GO, ex-G and a-ex-G demonstrated significantly improved ORR activity, showing a two-step reduction polarization curve common for graphitic carbon materials.^{12,34} The beneficial impact of nitrogen doping is clearly evidenced by the shift to a one step,

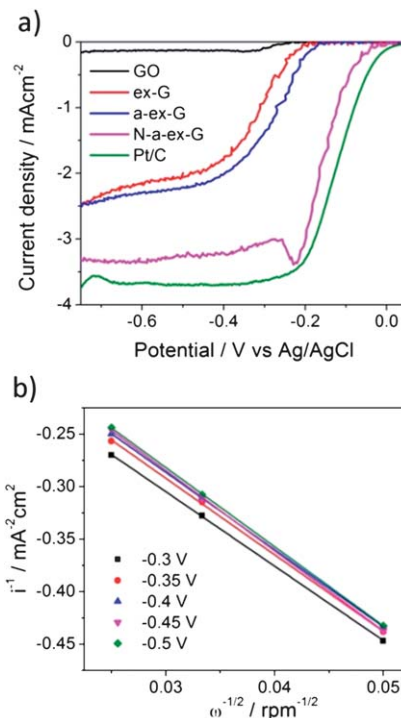


Fig. 4 Half-cell ORR evaluation obtained in an oxygen saturated 0.1 M KOH electrolyte at an electrode rotation of 900 rpm and a potential scan rate of 10 mV s^{-1} and (b) Koutecky–Levich plots for N-a-ex-G at varying electrode potentials.

predominant 4 electron ORR mechanism for N-a-ex-G with activity approaching state-of-the-art commercial Pt/C. Notably, the onset potential for N-a-ex-G was only *ca.* 45 mV lower than Pt/C. While activity approaching or exceeding Pt/C has been reported for nitrogen-doped carbon nanotubes or graphene synthesized in the presence of transition metal species,^{12,24,35} generally the performance in the absence of metallic species is much lower with some preferential formation of HO_2^- byproducts.^{36–38} Reports of metal-species free nitrogen doped graphene with activity approaching that of Pt/C are rare,⁷ indicating the promise of the present synthesis approach. A distinct reduction peak is also observed at $-0.21 \text{ V vs. Ag/AgCl}$, most likely due to the reduction of oxygen molecules adsorbed onto high surface area N-a-ex-G. Koutecky–Levich plots (discussion of analysis technique provided in the ESI†) for N-a-ex-G at varying electrode potentials are provided in Fig. 4b using electrode rotations of 400, 900 and 1600 rpm (100 rpm was excluded due to excessive noise contributions). These plots illustrate parallel, linear behaviour, which indicates first order reaction kinetics with respect to oxygen species.²⁵ Moreover, they provide indication of a predominant 4 electron reduction mechanism throughout the entire range investigated, along with steadily increasing kinetically limited current densities at decreasing electrode potentials. With the cost of N-a-ex-G being negligible in comparison to the soaring prices of Pt-based catalysts, the high ORR activity of N-a-ex-G renders it as a very promising and long term economical metal-air battery catalyst. While the half-cell performance provides an effective screening method for potential air electrode catalysts, it cannot provide an accurate

gauge of practical metal–air battery performance due to different operating conditions and catalyst morphology contributions. Thus, based on the promising half-cell ORR kinetics of N-a-ex-G, practical metal–air battery single-cell performance was investigated.

Fig. 5 provides the practical performance of an N-a-ex-G air electrode catalyst in a home-made zinc–air battery cell illustrated in detail in the ESI (Fig. S9a and b†). The discharge performance of a-ex-G and commercial Pt/C is included for comparison. Consistent with half-cell testing, the air electrode polarization curves (Fig. 5a) indicated that N-a-ex-G had significantly higher performance capabilities than a-ex-G, further confirming the importance of nitrogen doping. Specifically, the mass based current density of N-a-ex-G at 1.0 V was *ca.* 6 times higher than that of a-ex-G. Remarkably, the performance of N-a-ex-G was superior to Pt/C, whereby at the same battery potential N-a-ex-G demonstrated a 60% higher mass based discharge current. Zinc–air battery performances on an active electrode area basis (mA cm^{-2}) are provided in Fig. S9c.† Despite lower electrode catalyst loading for N-a-ex-G (1.63 mg), device performance approached that of Pt/C (2.58 mg) and was superior to that of a-ex-G (2.28 mg). This further verifies the promise of N-a-ex-G materials, whereby due to the minimal cost in comparison with Pt/C, electrode loadings can be increased without significant increase in costs in order to realize further practical enhancements. AC electrochemical impedance spectroscopy was carried out and fitted to the equivalent circuit provided in the inset of Fig. 5a. The Nyquist plot (Fig. 5b) demonstrated two semi circles, one at high frequency values and one at low frequency values; consistent observations for air

cathode impedance analyses.^{13,21,39} Three resistance values were obtained based on curve fitting and calculations as described in the ESI,† with results tabulated in Table S1.† Particularly, N-a-ex-G demonstrated a slightly higher charge transfer resistance than that of Pt/C, consistent with half-cell testing. Despite this, reduced ohmic and interfacial resistances were determined for N-a-ex-G which we suggest are due to the superior electronic conductivity of graphene based materials, along with the exemplary surface areas and properties of the N-a-ex-G catalyst. These factors provide reasonable explanation for the improved discharge current densities obtained for N-a-ex-G air electrodes, which will be crucial in order to provide high power densities to meet modern electronic demands.

The oxygen electrode performance of N-a-ex-G in a single cell lithium–oxygen battery was evaluated by galvanostatic testing (Fig. 6a), showing a typical flat discharge voltage profile followed by termination due to discharge product pore filling and electrode choking.^{40,41} N-a-ex-G displayed excellent discharge capacity ($11\,746\text{ mA h g}^{-1}$) for an electrode comprised of 20 wt% N-a-ex-G and the remaining ketjen black. This capacity was 42% higher than pure ketjen black, and furthermore, the cell voltage for N-a-ex-G was typically *ca.* 0.16 V higher during pseudo-steady state battery discharge. These enhancements are most likely due to the enhanced ORR kinetics of N-a-ex-G^{42,43} along with the immense surface areas and defect sites available to accommodate mass transport discharge product formation.^{9,44} After operation, the battery cell was disassembled under argon protection for XRD analysis (Fig. 6b), which confirmed successful Li_2O_2 discharge product

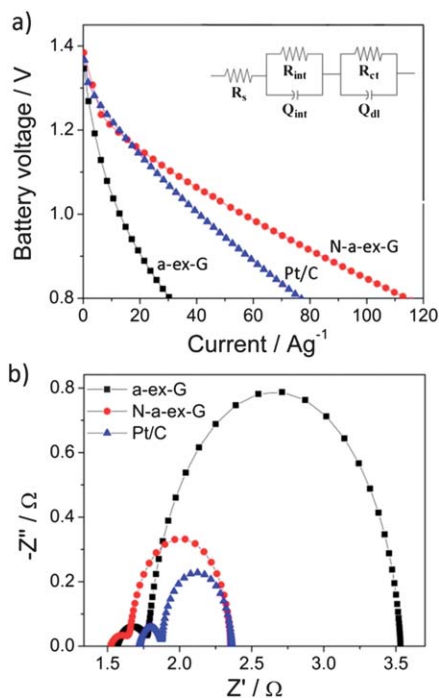


Fig. 5 Zinc–air battery (a) polarization curves and (b) Nyquist impedance plots of catalyst coated air electrodes. (Inset of a) Equivalent circuit used for impedance spectra fitting.

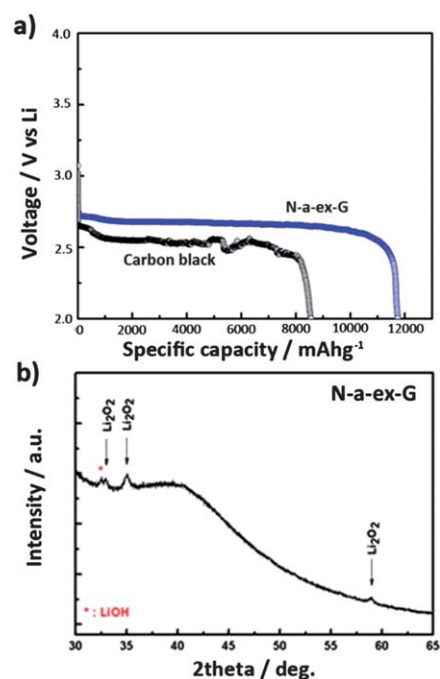


Fig. 6 Lithium–oxygen battery (a) discharge performance of N-a-ex-G/carbon black and pure carbon black electrodes at a discharge current of 70 mA g^{-1} , and (b) XRD pattern of N-a-ex-G following battery discharge demonstrating formation of Li_2O_2 discharge products, with trace amounts of LiOH observed due to imperfect sealing (moisture exposure) during handling and testing.

formation.⁴³ A small LiOH peak was also observed most likely due to imperfect sealing and moisture exposure during battery disassembly and XRD testing.

4 Conclusions and summary

Effectively and innovatively coupling KOH activation with nitrogen doping plays a crucial role in developing highly ORR active materials with exemplary surface areas and porosity. Drawing on these findings, N-a-ex-G has been demonstrated to provide excellent practical metal-air battery performance, evaluated using zinc-air and lithium-oxygen battery test cells. This unique approach opens up new and exciting opportunities for improvements in air electrode catalyst technologies for metal-air batteries in order to improve the performance and economic viability of these emerging electrochemical energy storage systems. N-a-ex-G is presented as a promising candidate for air cathode catalysts that can potentially replace traditionally used expensive Pt/C and transition metal complexes.

Acknowledgements

This work was financially supported by the Natural Sciences and Engineering Research Council of Canada (NSERC), the University of Waterloo and the Waterloo Institute for Nanotechnology. TEM images were obtained at the Canadian Centre for Electron Microscopy at McMaster University.

References

- 1 B. Winther-Jensen and D. R. MacFarlane, *Energy Environ. Sci.*, 2011, **4**, 2790–2798.
- 2 J.-S. Lee, S. Tai Kim, R. Cao, N.-S. Choi, M. Liu, K. T. Lee and J. Cho, *Adv. Energy Mater.*, 2011, **1**, 34–50.
- 3 D. S. Su, J. Zhang, B. Frank, A. Thomas, X. Wang, J. Paraknowitsch and R. Schlögl, *ChemSusChem*, 2010, **3**, 169–180.
- 4 Y. Zhu, S. Murali, W. Cai, X. Li, J. W. Suk, J. R. Potts and R. S. Ruoff, *Adv. Mater.*, 2010, **22**, 3906–3924.
- 5 Y. Shao, S. Zhang, M. H. Engelhard, G. Li, G. Shao, Y. Wang, J. Liu, I. A. Aksay and Y. Lin, *J. Mater. Chem.*, 2010, **20**, 7491–7496.
- 6 H. Wang, T. Maiyalagan and X. Wang, *ACS Catal.*, 2012, **2**, 781–794.
- 7 D. Geng, Y. Chen, Y. Chen, Y. Li, R. Li, X. Sun, S. Ye and S. Knights, *Energy Environ. Sci.*, 2011, **4**, 760–764.
- 8 E. Yoo, J. Nakamura and H. Zhou, *Energy Environ. Sci.*, 2012, **5**, 6928–6932.
- 9 Y. Li, J. Wang, X. Li, D. Geng, M. N. Banis, R. Li and X. Sun, *Electrochem. Commun.*, 2012, **18**, 12–15.
- 10 Z. Chen, D. Higgins and Z. Chen, *Carbon*, 2010, **48**, 3057–3065.
- 11 Z. Chen, D. Higgins and Z. Chen, *Electrochim. Acta*, 2010, **55**, 4799–4804.
- 12 K. Gong, F. Du, Z. Xia, M. Durstock and L. Dai, *Science*, 2009, **323**, 760–764.
- 13 Z. Chen, A. Yu, D. Higgins, H. Li, H. Wang and Z. Chen, *Nano Lett.*, 2012, **12**, 1946–1952.
- 14 D. Geng, S. Yang, Y. Zhang, J. Yang, J. Liu, R. Li, T.-K. Sham, X. Sun, S. Ye and S. Knights, *Appl. Surf. Sci.*, 2011, **257**, 9193–9198.
- 15 L. Sun, L. Wang, C. Tian, T. Tan, Y. Xie, K. Shi, M. Li and H. Fu, *RSC Adv.*, 2012, **2**, 4498–4506.
- 16 Z. Chen, D. Higgins, A. Yu, L. Zhang and J. Zhang, *Energy Environ. Sci.*, 2011, **4**, 3167–3192.
- 17 Y. Zhu, S. Murali, M. D. Stoller, K. J. Ganesh, W. Cai, P. J. Ferreira, A. Pirkle, R. M. Wallace, K. A. Cychosz, M. Thommes, D. Su, E. A. Stach and R. S. Ruoff, *Science*, 2011, **332**, 1537–1541.
- 18 D. Li, M. B. Muller, S. Gilje, R. B. Kaner and G. G. Wallace, *Nat. Nanotechnol.*, 2008, **3**, 101–105.
- 19 J. Díaz-Terán, D. M. Nevskaja, J. L. G. Fierro, A. J. López-Peinado and A. Jerez, *Microporous Mesoporous Mater.*, 2003, **60**, 173–181.
- 20 S.-H. Yoon, S. Lim, Y. Song, Y. Ota, W. Qiao, A. Tanaka and I. Mochida, *Carbon*, 2004, **42**, 1723–1729.
- 21 S. Zhu, Z. Chen, B. Li, D. Higgins, H. Wang, H. Li and Z. Chen, *Electrochim. Acta*, 2011, **56**, 5080–5084.
- 22 S. Hyoung-Oh, T. Yim, E. Pomerantseva and L. Nazar, *Electrochem. Solid-State Lett.*, 2011, **14**, A185–A188.
- 23 R. Pierotti and J. Rouquerol, *Pure Appl. Chem.*, 1985, **57**, 603–619.
- 24 Z. Chen, D. Higgins, H. Tao, R. S. Hsu and Z. Chen, *J. Phys. Chem. C*, 2009, **113**, 21008–21013.
- 25 D. Higgins, Z. Chen and Z. Chen, *Electrochim. Acta*, 2011, **56**, 1570–1575.
- 26 L. Lai, J. Potts, D. Zhan, L. Wang, C. K. Poh, C. Tang, H. Gong, Z. Shen, J. Lin and R. Ruoff, *Energy Environ. Sci.*, 2012, **5**, 7936–7942.
- 27 H. Niwa, K. Horiba, Y. Harada, M. Oshima, T. Ikeda, K. Terakura, J.-i. Ozaki and S. Miyata, *J. Power Sources*, 2009, **187**, 93–97.
- 28 C. V. Rao, C. R. Cabrera and Y. Ishikawa, *J. Phys. Chem. Lett.*, 2010, **1**, 2622–2627.
- 29 G. Eda and M. Chhowalla, *Adv. Mater.*, 2010, **22**, 2392–2415.
- 30 A. Kaniyoor, T. T. Baby and S. Ramaprabhu, *J. Mater. Chem.*, 2010, **20**, 8467–8469.
- 31 N. Shimodaira and A. Masui, *J. Appl. Phys.*, 2002, **92**, 902–909.
- 32 D. C. Higgins, D. Meza and Z. Chen, *J. Phys. Chem. C*, 2010, **114**, 21982–21988.
- 33 C. Zhang, L. Fu, N. Liu, M. Liu, Y. Wang and Z. Liu, *Adv. Mater.*, 2011, **23**, 1020–1024.
- 34 D. C. Higgins, J. Wu, W. Li and Z. Chen, *Electrochim. Acta*, 2012, **59**, 8–13.
- 35 Q. Liu, H. Zhang, H. Zhong, S. Zhang and S. Chen, *Electrochim. Acta*, 2012, **81**, 313–320.
- 36 Z. Lin, M.-k. Song, Y. Ding, Y. Liu, M. Liu and C.-p. Wong, *Phys. Chem. Chem. Phys.*, 2012, **14**, 3381–3387.
- 37 Z. Lin, G. Waller, Y. Liu, M. Liu and C.-P. Wong, *Adv. Energy Mater.*, 2012, **2**, 884–888.

- 38 Y. Zhang, K. Fugane, T. Mori, L. Niu and J. Ye, *J. Mater. Chem.*, 2012, **22**, 6575–6580.
- 39 D. Thiele and A. Züttel, *J. Power Sources*, 2008, **183**, 590–594.
- 40 T. Ogasawara, A. Débart, M. Holzapfel, P. Novák and P. G. Bruce, *J. Am. Chem. Soc.*, 2006, **128**, 1390–1393.
- 41 L. Zhang, X. Zhang, Z. Wang, J. Xu, D. Xu and L. Wang, *Chem. Commun.*, 2012, **48**, 7598–7600.
- 42 Y. Li, J. Wang, X. Li, J. Liu, D. Geng, J. Yang, R. Li and X. Sun, *Electrochem. Commun.*, 2011, **13**, 668–672.
- 43 Y.-C. Lu, D. G. Kwabi, K. P. C. Yao, J. R. Harding, J. Zhou, L. Zuin and Y. Shao-Horn, *Energy Environ. Sci.*, 2011, **4**, 2999–3007.
- 44 Z.-L. Wang, D. Xu, J.-J. Xu, L.-L. Zhang and X.-B. Zhang, *Adv. Funct. Mater.*, 2012, **22**, 3699–3705.